Proceedings of the ASME 2020 International Design Engineering Technical Conferences & Computers and Information in Engineering Conference
IDETC/CIE 2020
August 16-August 19, 2020, St. Louis, MO, USA

DETC2020-18707

VISUALISING COMPLIANCE OF COMPOSITE SHELL MECHANISMS

Jonathan P. Stacey*
Matthew P. O'Donnell
Mark Schenk
Bristol Composites Institute (ACCIS)
Department of Aerospace Engineering
University of Bristol
Bristol, BS8 1TR, United Kingdom
Email: jonathan.stacey@bristol.ac.uk

Charles J. Kim
Department of Mechanical Engineering
Bucknell University
Lewisburg, PA 17837, USA
Email: charles.kim@bucknell.edu

ABSTRACT

In the design of isotropic compliant shell-based mechanisms a desired response of an end-effector is commonly achieved through careful selection of shell geometry and material. However, for applications such as the design of medical support devices the shell must conform to a highly constrained set of permissible geometries, limiting tailorability. One solution to this design challenge is to exploit anisotropic material behaviour.

Advanced composite materials may be elastically tailored by varying the fibre orientation, but at the cost of increased design complexity. Herein we present an approach for capturing the effects of material anisotropy on compliant shell mechanisms by providing the designer with a method for visualising their response in a physically intuitive manner.

We extend the mechanism characterisation technique of Lipkin and Patterson [1] using eigen-decomposition, and visualise the compliance vectors for structures with material anisotropy. We characterise the behaviour of cantilevered "tape-spring" shell geometries with varying enclosed angles using nonlinear finite element analysis. For small enclosed angles we observe significant reorienting of the compliance vectors due to stiffness anisotropy; as the enclosed angle is increased, geometry dominates the response. However, in an intermediate region both geometric and stiffness effects interact, highlighting the potential richness of the design space.

INTRODUCTION

Compliant mechanisms utilise elastic structural deformations in place of traditional mechanical features, such as joints and hinges, to transmit forces or displacements. Such compliant mechanisms offer several advantages over traditional designs, such as decreased part count, elimination of friction and need for lubrication, and opportunities to introduce preferable manufacturing techniques [2]. The geometry and topology of compliant mechanisms can be readily tailored to obtain desirable responses, see *e.g.* Refs. [3–5]. However, despite their potential advantages, the design of compliant mechanisms remains challenging, in part due to the complexity associated with describing the typically nonlinear response.

Compliant mechanism design often relies upon optimising the geometry of isotropic thin-walled shell structures, see for instance Refs. [6–8]. However, for many applications freedom to select desirable shell geometry is significantly reduced. For example, a scoliosis brace must be of an anatomically desirable form, fitting closely to the patient's body [9,10]. Advanced composite materials offer a potential solution in these instances by providing a light-weight, anisotropically tailorable material system that offers increased design freedom and deformation control, without changing the shell's geometry [11].

Composite materials have found many applications within the morphing and nonlinear structures fields, see *e.g.* Refs. [12–15]. Through careful tailoring of structural form and the

*Address all correspondence to this author

composites' anisotropic stiffness, bespoke nonlinear responses can be readily achieved. Despite composites' many advantages, their use in the design of compliant mechanisms is currently under-utilised, with prior investigations typically restricted to planar mechanisms [16, 17]. This can be partially attributed to the increased complexity of the design space, making physical intuition into the expected response more elusive. In order to mitigate this limitation, we propose a new visual characterisation approach that offers increased physical insight into the various compliant responses. In particular, our approach captures the transition from stiffness to geometry-dominated regimes and the intermediate behaviours. Such a tool permits the designer to identify shell geometries where stiffness tailoring can provide a significant increase in range of response.

This paper expands a shell compliance visualisation technique based on eigen-decomposition [1, 18–20], to include anisotropic materials. To illustrate our methodology, which may be applied to more general geometries a simple cantilever "tape-spring" with an applied tip-moment is used as a benchmark shell mechanism. The compliance behaviour of this mechanism is visualised and discussed for a case with an equivalent isotropic composite laminate, as well as highly-anisotropic composite laminates, for different geometries. The isotropic and highly-anisotropic cases are qualitatively compared and discussed. We identify regions of the design space that are stiffness or geometry-dominated and highlight the complex behaviour observed in mixed responses.

EIGEN-DECOMPOSITION

The visualisation technique we present herein is based on the eigen-decomposition analysis framework developed by Lipkin and Patterson [1]. Screw theory is utilised to determine the primary compliance directions (and associated magnitudes) of an elastic mechanism. These values are determined through analysis of the tangent stiffness matrix, derived from nonlinear finite element analysis, of a point of interest (POI) lying on the mechanism. As the mechanism undergoes large, nonlinear elastic deformations, the orientations, positions and magnitudes of primary compliance directions are tracked. These may be plotted and compared throughout the mechanism's large deformation (see Ref. [21] for an example of this with isotropic shells).

The approach is advantageous in providing physical insight into the behaviour of the mechanism because the behaviour of the POI can be readily interpreted with minimal knowledge of mechanism design — only an instinctive feel for compliance is needed. Despite these advantages, to the best of the authors' knowledge, this technique has not previously been applied to anisotropic composite shells.

Wrenches and Twists

Lipkin and Patterson's technique builds on Chasles' Theorem [22] which states that any movement in three dimensional space can be described by a translation along a line plus a rotation about the same line. In this framework the kinetics of a body are expressed as a vector combining forces and moments acting on and about a common axis. This is known as a wrench,

$$\boldsymbol{w} = \begin{bmatrix} \boldsymbol{f}_i \\ \boldsymbol{\tau}_i \end{bmatrix} = \begin{bmatrix} \boldsymbol{f}_i \\ (\boldsymbol{b}_i \times \boldsymbol{f}_i) + d_i \boldsymbol{f}_i \end{bmatrix}, \tag{1}$$

where $\boldsymbol{f}_i$ and $\boldsymbol{\tau}_i$ are the linear force and angular torque components of the wrench respectively, the $\boldsymbol{b}_i$ terms determine the spatial positioning, and d_i are the ratios of torque and force. The subscript $i \in [1,2,3]$, distinguishes each orthogonal wrench axis.

Similarly, the kinematics of the body can be expressed in terms of a vector combining translations and rotations about a common axis. This is known as a twist,

$$\boldsymbol{T} = \begin{bmatrix} \boldsymbol{\delta}_i \\ \boldsymbol{\gamma}_i \end{bmatrix} = \begin{bmatrix} (\boldsymbol{r}_i \times \boldsymbol{\gamma}_i) + h_i \boldsymbol{\gamma}_i \\ \boldsymbol{\gamma}_i \end{bmatrix}, \tag{2}$$

where $\boldsymbol{\delta}_i$ and $\boldsymbol{\gamma}_i$ are the translation and rotation components of the twist, $\boldsymbol{r}_i$ the location vector (taken as the shortest (*i.e.* perpendicular) distance between the twist vector and the POI) and h_i the pitch scalar with i distinguishing between three orthogonal twist axes.

Tangential Stiffness Matrix

The tangent stiffness and compliance matrices of a POI on the mechanism are decomposed into an eigen-system using the method described by Lipkin and Patterson [1]. For a tangent stiffness matrix this is

$$\boldsymbol{K}_t = \begin{bmatrix} \boldsymbol{K}_{11} & \boldsymbol{K}_{12} \\ \boldsymbol{K}_{21} & \boldsymbol{K}_{22} \end{bmatrix} = \begin{bmatrix} \hat{\boldsymbol{w}}_f & \hat{\boldsymbol{w}}_\gamma \end{bmatrix} \begin{bmatrix} k_f & 0 \\ 0 & k_\gamma \end{bmatrix} \begin{bmatrix} \hat{\boldsymbol{w}}_f^T \\ \hat{\boldsymbol{w}}_\gamma^T \end{bmatrix}, \tag{3}$$

where $\boldsymbol{K}_t$ is the 6×6 tangent stiffness matrix for the POI, $\hat{\boldsymbol{w}}_f$ and $\hat{\boldsymbol{w}}_\gamma$ the normalised translational and rotational components of the wrench respectively, and k_f and k_γ the corresponding stiffnesses (in the directions of f and γ). For a tangent compliance matrix this is,

$$\boldsymbol{C}_t = \begin{bmatrix} \boldsymbol{C}_{11} & \boldsymbol{C}_{12} \\ \boldsymbol{C}_{21} & \boldsymbol{C}_{22} \end{bmatrix} = \begin{bmatrix} \hat{\boldsymbol{T}}_f & \hat{\boldsymbol{T}}_\gamma \end{bmatrix} \begin{bmatrix} a_f & 0 \\ 0 & a_\gamma \end{bmatrix} \begin{bmatrix} \hat{\boldsymbol{T}}_f^T \\ \hat{\boldsymbol{T}}_\gamma^T \end{bmatrix}, \tag{4}$$

where $\boldsymbol{C}_t$ is the 6×6 tangent compliance matrix for the POI, $\hat{\boldsymbol{T}}_f$ and $\hat{\boldsymbol{T}}_\gamma$ the normalised translational and rotational components

of the twist respectively, and a_f and a_γ the corresponding compliances (in the directions of $\boldsymbol{f}$ and $\boldsymbol{\gamma}$).

This decomposition results in three translational and three rotational principal axes (and the corresponding stiffnesses). These are, $\boldsymbol{w}_f$, the eigen-wrenches (also known as wrench axes), and $\boldsymbol{T}_\gamma$, the eigen-twists (also known as twist axes). To compute this decomposition the eigenvectors ($\boldsymbol{v}$) and eigenvalues ($\boldsymbol{\lambda}$) of the upper-left (*i.e.* pure translational) quadrant ($\boldsymbol{K}_{11}$) of the 6×6 reduced stiffness matrix must be obtained, as well as those for the lower-right (*i.e.* pure rotational) quadrant ($\boldsymbol{C}_{22}$) of the 6×6 reduced compliance matrix. The eigenvectors correspond to the orientations of the twist and wrench axes, while the eigenvalues will give the corresponding stiffness or compliances along those axes. By definition, applying an eigenwrench to a system along its axis causes an induced twist of pure translation of the POI parallel to that axis. As such, multiplying the eigenvectors, $\boldsymbol{v}_{K_t}$, by the corresponding $\boldsymbol{K}_t$ stiffness matrix quadrants gives expressions for the eigenwrenches,

$$\boldsymbol{w}_f = \boldsymbol{v}_{K_t} * \begin{bmatrix} \boldsymbol{K}_{11} \\ \boldsymbol{K}_{21} \end{bmatrix} \tag{5}$$

Similarly, applying an eigentwist along its axis will cause an induced wrench of pure moment to occur around the POI, parallel to the twist axis direction. These twist axes are expressed with the corresponding C_t compliance matrix terms and eigenvectors $\boldsymbol{v}_{C_t}$ as

$$\boldsymbol{T}_\gamma = \boldsymbol{v}_{C_t} * \begin{bmatrix} \boldsymbol{C}_{12} \\ \boldsymbol{C}_{22} \end{bmatrix} \tag{6}$$

Conceptually, applying eigentwists and eigenwrenches to a system is akin to applying a load or displacement to a rigid body connected to the POI, rather than to the indicated location on the shell.

Anisotropic Material Stiffness

For thin composite structures, classical laminate theory (CLT), provides a robust method for determining the stiffness matrix of the shell structure. This captures the orientation of the fibres, as well as the order in which these are laid up to produce the composite laminate material. The laminate's in-plane, $\boldsymbol{A}$, coupling $\boldsymbol{B}$ and bending stiffness $\boldsymbol{D}$ matrices (see Ref. [23]) contribute to $\boldsymbol{K}_t$ and $\boldsymbol{C}_t$ of the shell mechanism. For the symmetric tape spring, the laminate's bending-torsion coupling terms D_{16} and D_{26} contribute to off axis quadrants, $\boldsymbol{K}_{21}$ and $\boldsymbol{C}_{12}$, capturing the out-of-plane deformation behaviour caused by the material anisotropy.

Normalised Orientations

The eigenwrenches, $\boldsymbol{w}_f$, and eigentwists, $\boldsymbol{T}_\gamma$, are normalised by their respective eigenvalues to complete the decomposition.

The normalised orientations ($\hat{\boldsymbol{w}}_f$ and $\hat{\boldsymbol{T}}_\gamma$) and compliance magnitudes ($\boldsymbol{\lambda}_f$ and $\boldsymbol{\lambda}_\gamma$) describe the six principal translational and rotational axes of the POI. In order to determine the placement of these axes in space, their position vectors, $\boldsymbol{r}_i$, relative to the POI must be found. For example, to find the twist axes' vectors, $\boldsymbol{r}_{\text{twists}}$, the following process is implemented. We define the twist pitch scalar as,

$$h_i = \boldsymbol{\delta}_i \cdot \boldsymbol{\gamma}_i, \tag{7}$$

with $\boldsymbol{\delta}_i$ and $\boldsymbol{\gamma}_i$ taken from the upper half and lower half of $\hat{\boldsymbol{T}}_\gamma$ respectively. The twist position vectors, $\boldsymbol{r}_{\text{twists}}$ are calculated via the vector triple product identity,

$$\boldsymbol{\gamma}_i \times (\boldsymbol{r}_{\text{twists}} \times \boldsymbol{\gamma}_i) = (\boldsymbol{\gamma}_i \cdot \boldsymbol{\gamma}_i)\boldsymbol{r}_{\text{twists}} - (\boldsymbol{\gamma}_i \cdot \boldsymbol{r}_{\text{twists}})\boldsymbol{\gamma}_i, \tag{8}$$

which can be simplified, noting that $\boldsymbol{r}_i$ is orthogonal to $\boldsymbol{\gamma}_i$ by its definition as the shortest distance from the POI to the twist vector,

$$-(\boldsymbol{r}_{\text{twists}} \times \boldsymbol{\gamma}_i) \times \boldsymbol{\gamma}_i = |\boldsymbol{\gamma}_i|^2 \boldsymbol{r}_{\text{twists}}, \tag{9}$$

and combined with the definition of $\boldsymbol{\delta}_i$ from (2), giving

$$\frac{-(\boldsymbol{\delta}_i - h_i\boldsymbol{\gamma}_i) \times \boldsymbol{\gamma}_i}{|\boldsymbol{\gamma}_i|^2} = \boldsymbol{r}_{\text{twists}}. \tag{10}$$

A similar process allows the definition of the wrench axes vectors, $\boldsymbol{r}_{\text{wrenches}}$, using d_i, $\boldsymbol{b}_i$, $\boldsymbol{f}_i$ and $\boldsymbol{\tau}_i$, but is not included for brevity. Thus the orientations ($\hat{\boldsymbol{w}}_f$ and $\hat{\boldsymbol{T}}_\gamma$), compliance magnitudes ($\boldsymbol{\lambda}_f$ and $\boldsymbol{\lambda}_\gamma$), and positions ($\boldsymbol{r}_{\text{wrenches}}$ and $\boldsymbol{r}_{\text{twists}}$) for the six principal translational and rotational axes of the POI are defined and the compliance behaviour can be now be visualised. We proceed to outline an example of the implementation using finite element analysis.

IMPLEMENTATION: A FINITE ELEMENT APPROACH

A series of tape spring shell mechanisms with selected anisotropic material properties (see Figure 1) are analysed to demonstrate the visualisation of the principal compliance axes. These provide a simple geometry which is applicable to biomedical support applications. Specifically, small tape springs were investigated (chord $c = 5$ mm, thickness $h = 0.5$ mm, and aspect ratio $a = L/c = 2$) to represent shell mechanisms for segments of finger braces or precision mechanisms.

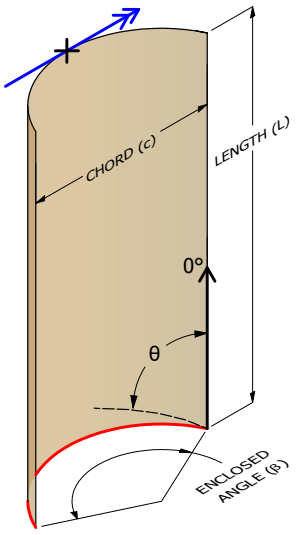

FIGURE 1: TAPE SPRING GEOMETRY, WITH LOCATION OF POI (+), APPLIED MOMENT (BLUE ARROW), ENCASTRE BOUNDARY CONDITION (RED EDGE), AND COMPOSITE FIBRE ANGLE θ.

Analysis Method

Cantilevered tape springs shell structures subject to a follower moment acting on the POI were analysed using Abaqus/Standard 2018 using S4R shell elements. This follower moment was chosen to reflect a finger brace load case. A mesh density of six elements per millimetre of shell chord, c, and length, L, was selected after a mesh convergence study for POI displacement. The POI is located at the centre of the tip edge, as shown in Figure 3a, and a rigid body constraint was applied to all tip edge nodes to ensure they displaced with the POI.

In order to compare behaviour for a range of anisotropic material properties, a common energetic input is enforced to limit the magnitude of the applied moment: the same work is done in all cases. A limit of 0.1 J was selected following inspection of preliminary results; this value gave appropriately large deformations without entering extreme response modes. No material failure was implemented, so deformations were not limited by developed stresses or strains.

To reach the prescribed energetic input, the shells were incrementally loaded using a series of nonlinear static analyses, and POI stiffness matrices were extracted using a substructure analysis (see Figure 2 for the analysis process). The local stiffness matrices and deformed shell geometries for each loading step are subsequently post-processed via MATLAB to calculate the eigen-decomposition and produce the visualisation of shell compliance.

TABLE 1: MATERIAL DATA E-GLASS / EPOXY [24]

$E_{11} = 41$ GPa	$G_{12} = 4.3$ GPa
$E_{22} = 10.4$ GPa	$\nu_{12} = 0.28$
$E_{11}/E_{22} = 3.9$	$h = 0.5$ mm

Material Properties

An E-Glass/Epoxy material system was selected for investigation [24]; see Table 1. This material system provides a sufficient level of anisotropy ($E_{11}/E_{22} \approx 4$) to illustrate the different modes of behaviour that can be achieved when compared to an isotropic material. The ratio of stiffness along fibre E_{11} and transverse E_{22} directions dictates the relative magnitudes of deformation of the POI. This further depends on the orientation of the anisotropy, described by fibre angle θ with respect to the tape spring's longitudinal axis (see length, L, in Figure 1).

For materials such as carbon-fibre reinforced polymers with increased anisotropy ($E_{11}/E_{22} \approx 15$), the difference in magnitude of POI deformations between the low and high compliance orientations can be of an order of magnitude different. Although this presents a challenge when comparing responses, it highlights the potential of elastic tailoring to improve performance for fixed shell geometries. Thus, the results presented herein should not be considered the extremes of the potential design space.

To provide an isotropic benchmark, an eighteen-ply laminate that exhibits equivalent isotropic properties is used [25]; see Table 2. This means that the fibre angles and stacking sequence cause the laminate to exhibit isotropic behaviour, in this case equivalent in-plane and bending moduli of $E = 20.6$ GPa. Mechanisms utilising this fully isotropic laminate were compared with those containing highly-anisotropic single-ply angle laminates (each with a single fibre angle) of the same total laminate thickness for two values of enclosed tape spring angle.

TABLE 2: LAMINATE LAYUPS INVESTIGATED

Cases	Layup
Isotropic benchmark	[0° -60° 60° 0° -60° 60°$_3$ −60°$_2$ 0°$_2$ -60° 0°$_2$ 60°$_2$ -60°]
Single fibres	[0°], [30°], [45°], [60°], [90°]

VISUALISATION OF COMPLIANCE

Figures 3–5 show the resulting visualisation of the shell's compliance analysis, for three case studies. The aim is to provide an overview of the magnitudes and (re)orientation of the twist and wrench axes throughout the deformation of the compliant shell mechanisms. Combining this information helps inform the

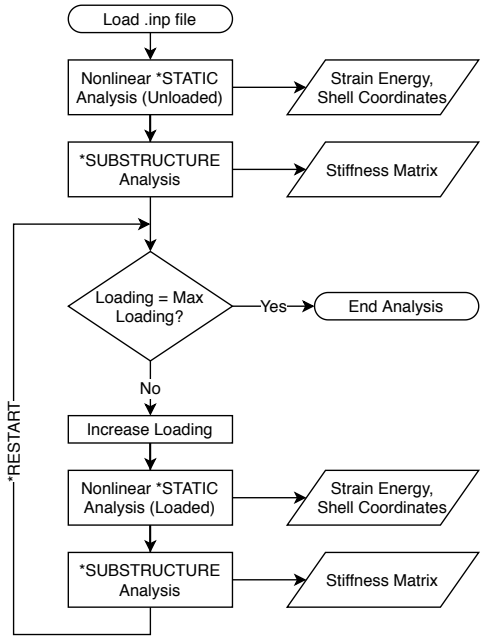

FIGURE 2: Finite element analysis process

mechanism designer about the effect of parameters such as shell geometry and material anisotropy. To achieve this, each figure consists of five sub-plots:

(a) **Deformed and undeformed configurations**: a 3D representation of the shell in its original and fully-deformed state, including twist and wrench axes for the original state.

Sub-plot (a) gives the designer insight into the spatial movement of the whole shell as well as the POI, which can include bending-torsion motion in anisotropic cases. Visualising the initial (pre-deformation) positions and orientations of the twist and wrenches provides an indication of the shell's characteristics when subject to small deformation load-cases.

(b) **Wrench axes**: a polar plot shows the (re)orientation of the wrenches throughout the mechanism deformation.

(c) **Twist axes**: a polar plot shows the (re)orientation of the twists throughout the mechanism deformation.

Sub-plots (b) and (c) are polar plots that illustrate orientations of the twist and wrench vectors. The plots are akin to looking at one half of a unit sphere upon which lie traces of the axes emanating from its centre, and do not contain any information about the positions of the axes in space. The initial, undeformed, vector orientations together with the final values are marked to aid interpretation of realignment under loading. The polar-plots are included to help illustrate how the alignment of principal axes may favour or restrict a deformation path, as well as how this changes with different laminates.

(d) **Wrench compliances**: a plot showing the variation in compliance magnitudes of the wrenches.

(e) **Twist compliances**: a plot showing the variation in compliance magnitudes of the twists.

Subplots (d) and (e) show compliance magnitudes plotted against applied work. These plots illustrate the most compliant axes, the relative compliance between axes, and how these change throughout the mechanism deformation. This is particularly useful for the designer in cases where initial compliances between some wrenches or twists are similar, or where there are sudden changes in compliance (*e.g.* the development of a fold in a tape spring hinge).

Figures 3–5 each compare the results for three cases with different material anisotropy. Figure 3 investigates a shallow tape spring (enclosed angle $\beta = 15°$) with a 0°, 90° and an isotropic laminate. Figure 4 compares mechanisms with the same geometry, but a 30°, 45°, and 60° laminate. Figure 5 replicates Figure 4, but for mechanisms with a larger curvature ($\beta = 45°$).

Case I: Isotropy & Aligned Anisotropy

Figure 3 compares the behaviour of the equivalent isotropic laminate with the most extreme form of stiffness anisotropy that can be achieved with the specified material system (0° or 90° laminates).

Figure 3a shows a representative shell deformation for the $\theta = 90°$ laminate. Due to the geometric and material symmetry of the shell mechanism in the undeformed configuration, the twist and wrench axes are parallel to the tape spring chord and longitudinal axes. Note that in the plotted 90° case, the twist and wrench axes overlap visually, and while parallel they are not coincident: w_1 (red) with T_1 (blue), w_2 (brown) with T_3 (green), and w_3 (yellow) with T_2 (teal). They also remain parallel during deformation, as shown in Figures 3b–3c, as no geometric or material asymmetry exists.

Figures 3d–3e identify w_1 and T_3 as the most compliant wrench and twist axes, respectively, for all cases shown. For the 90° and isotropic cases, these map to a transverse load resulting in cantilever bending (w_1) and a bending mode parallel to the tape spring chord axis (T_3). Note that the wrench axis is not placed at the POI: a load applied there would induce both translation and rotation, whereas a load along the plotted w_1 axis only produces a translation of the POI. The torsional T_2 twist axis passes nominally through the shear centre of the cantilevered tape spring, as this provides the instantaneous rotation axis of the cross-section. Note that wrench w_2 is parallel to the chord axis and is applied through the shear centre of the cross-section as this will induce no torsion.

For the 0° case T_3 is still the most compliant twist, but it

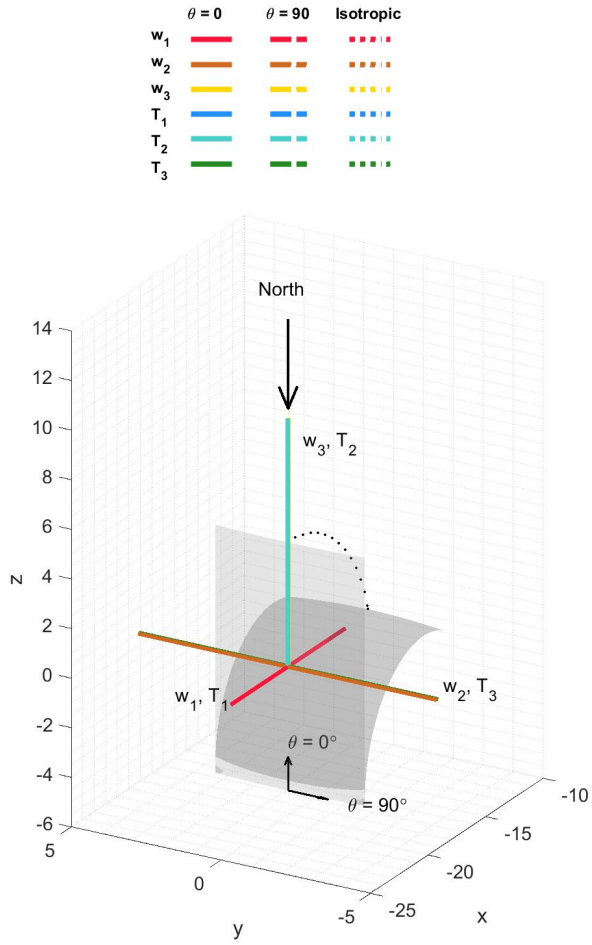

(a) DEFORMED (DARK) AND UNDEFORMED (LIGHT) SHELLS, POI LOCATIONS (•) AND UNDEFORMED TWIST AND WRENCH AXES. $\theta = 90°$.

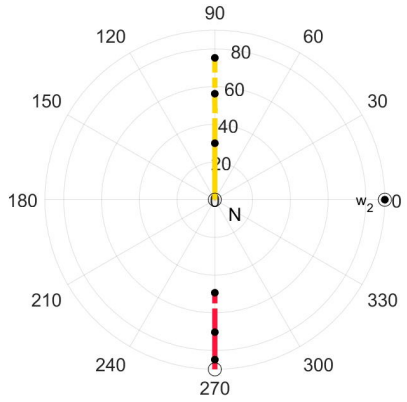

(b) WRENCH AXIS ORIENTATION CHANGES, AS SEEN FROM 'NORTH' DIRECTION. MARKERS INDICATE: UNDEFORMED STATES (○) AND FULLY-DEFORMED STATES (•).

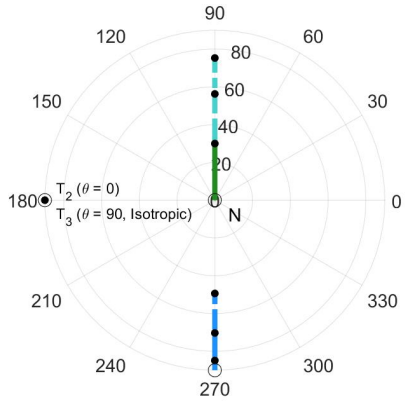

(c) TWIST AXIS ORIENTATION CHANGES, AS SEEN FROM 'NORTH' DIRECTION. MARKERS INDICATE: UNDEFORMED STATES (○) AND FULLY-DEFORMED STATES (•).

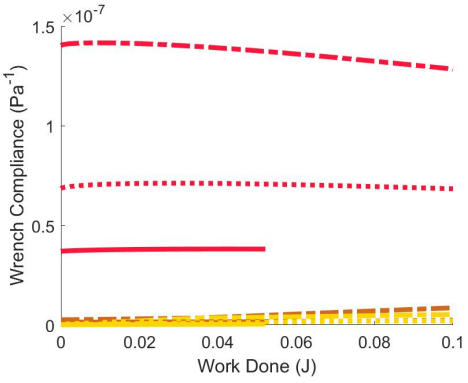

(d) WRENCH COMPLIANCE MAGNITUDE CHANGES

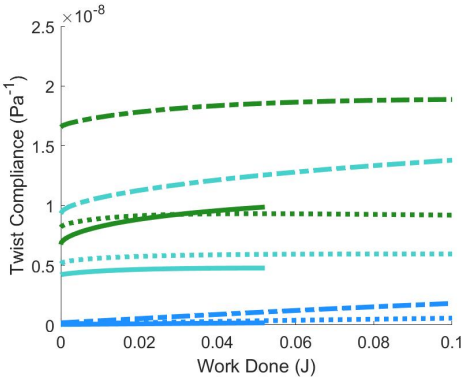

(e) TWIST COMPLIANCE MAGNITUDE CHANGES

FIGURE 3: VISUALISATION OF COMPLIANCE BEHAVIOUR FOR SINGLY-CURVED (ENCLOSED ANGLE 15°), ASPECT RATIO 2 SHELL MECHANISMS COMPRISED OF FULLY ISOTROPIC, $\theta = 0°$, OR $\theta = 90°$ LAMINATES.

is now aligned with the tape spring torsion axis. In both the 0° and 90° cases T_3 aligns with the fibre direction, showing an anisotropic stiffness-dominated behaviour that favours rotation about the fibres. For cases with extreme β angles (*e.g.* $\beta >= 180°$, not shown here for brevity), the behaviour becomes geometry-dominated, with rotation around the tape spring torsion axis always favoured. The 0° case was only plotted up to a strain energy of approximately 0.05 J as numerical instabilities occurred in the finite element model when the shell was loaded beyond this point.

In the isotropic case, T_3 favours tape spring bending rotation over torsional rotation, due to the short aspect ratio increasing the influence of the encastre boundary conditions. The compliance magnitude of T_2 (torsion) and T_3 (bending) twist axes are similar though; increasing enclosed angle β would separate these compliances. Twist T_3 is the only axis marginally more compliant in the 0° case compared to the isotropic case due to the fibres being aligned along the tape spring torsion axis.

As all the shell cases deform, the w_1 wrench compliance gradually decreases as the increasingly curved geometries cause the perpendicular distance between w_1 and the encastre edge to decrease. As the mechanism bends, however, the shell transverse curvature decreases towards the centre of the longitudinal axis, which can be seen in the increase in rotational compliance of the bending twist, particularly in the 90° case. This is due to Poisson's ratio effects causing the curved shell to 'open out'. This effect is directly related to fibre orientation as, for example, a 90° laminate will have a much smaller Poisson's ratio than a 0° laminate, causing the shell to 'open-out' more. Applying further work to the shell would result in a tape spring fold developing (*i.e.* this mid-spring curvature reducing to zero), characterised by a rapid increase in T_2 compliance.

For all cases, wrenches w_2 and w_3 (shear and axial loading) and twist T_1 have comparatively very low compliance and consequently have a much smaller impact on the mechanism behaviour. The ordering of the compliances does not change during the deformation of the shell.

Case II: Non-Aligned Anisotropy: Small Curvature

Figure 4 compares the compliance behaviour throughout deformation for the geometry shells as Figure 3, except that they now are made from composite laminates comprised of a single fibre angle. The angles of 30°, 45° and 60° were chosen to show a broad range of behaviour between the previously shown 0° and 90° cases.

Figure 4a shows a representative shell deformation for the $\theta = 30°$ case. It can now be seen the twist and wrench axes no longer align with the geometric axis (or with each other), as in Figure 3, due to the laminate's material anisotropy. In addition, only w_1 (red) and T_1 (blue) remain approximately parallel during deformation as shown in Figures 4b–4c as they both remain closely parallel to the shell normal direction.

Figure 4d–4e shows that, like the cases in Figure 3, the most compliant wrench and twist are w_1 (red) and T_3 (green) respectively. It can be seen that upon loading there is a brief peak in w_1 compliance, before it decreases with further loading; larger fibre angle laminates exhibit higher compliances. During deformation the mechanism undergoes a bending-torsion deformation which briefly makes w_1 more compliant. The initial orientation of T_3 favours alignment with the fibres (similarly to Figure 3), but shell curvature and boundary conditions also have an effect, so the alignment is orientated at higher angle than the fibre direction. Again, upon loading there is a brief peak in T_3 compliance (due to opening of shell curvature) before a more gradual decrease with further loading. The local rotation of T_3 is confined mostly to out-of-plane motion not captured in Figure 4c using the current northerly view.

Unlike the 90° case in Figure 3e, the T_3 compliances remain approximately twice as compliant as T_2 (teal). This is because T_3 is no longer parallel to the shell chord axis as in the 90° case, and thus the geometric stiffness from curvature does not dominate T_3 as much. With the introduction of symmetry breaking due to non-aligned fibre orientations we observe a bend-torsion mode of deformation not seen in Case I. The coupled bending-torsion (governed primarily by T_3), illustrates a stiffness-dominated response unobtainable in a similar shell with isotropic materials.

In purely stiffness-dominated behaviours the initial compliance magnitudes reduce or increase depending on the axes' proximity to the fibre orientation. As the enclosed angle of the tape spring curvature increases to extreme values, the geometry effects can dominate the stiffness behaviour again, and the twist axes can align much better with the classical tape spring axes, even in the presence of non-aligned material anisotropy.

Similarly to Figure 3 wrenches w_2 (orange) and w_3 (yellow) are much less compliant than w_1, so would have little effect on the shell behaviour even though the bending-torsion deflection causes large changes in their orientations.

Case III: Non-Aligned Anisotropy: Large Curvature

Figure 5 shows the compliance behaviour for the same composite laminates as Figure 4, with increased enclosed angle $\beta = 45°$ resulting in larger transverse curvature. Figure 5a shows a representative shell deformation for the $\theta = 30°$ case, showing that the final deformation is reduced with the increased β due to the geometric stiffening it provides.

Figure 5d–5e shows that, like the cases in Figures 3–4, the most compliant wrench and twist are w_1 (red) and T_3 (green) respectively. The increase in shell curvature has reduced the peak compliance magnitudes of w_1, however, as the tape spring cross-section has a greater second moment of area and provides greater resistance to cantilever bending, and a less deformed shell for the same energy. The w_1 compliance increase during deformation is

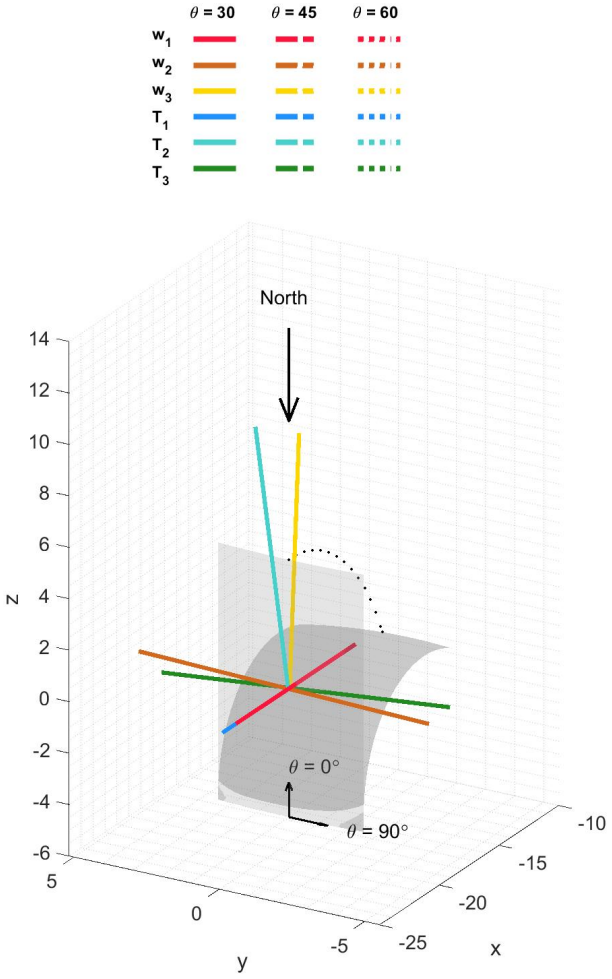

(a)

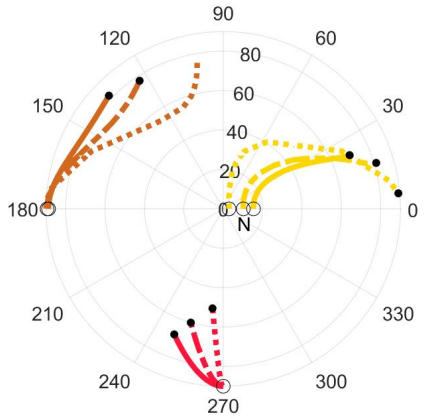

(b)

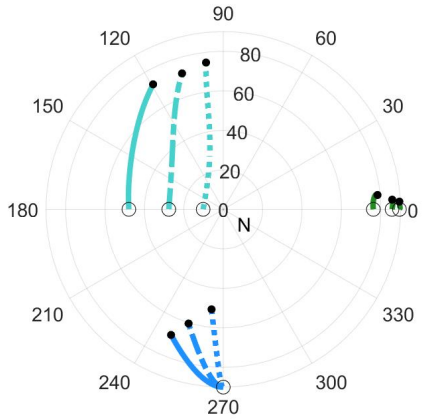

(c)

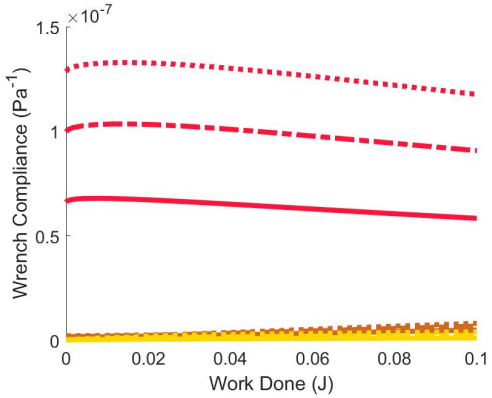

(d)

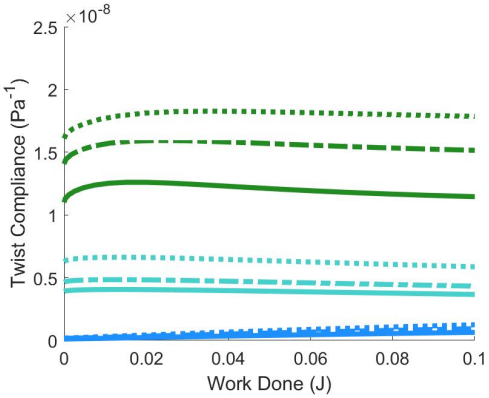

(e)

FIGURE 4: VISUALISATION OF COMPLIANCE BEHAVIOUR FOR SINGLY-CURVED TAPE SPRING ($\beta = 15°$, $a = 2$) SHELL MECHANISMS COMPRISED OF $\theta = 30°$, $\theta = 45°$, OR $\theta = 60°$ LAMINATES. FIGURE (A) SHOWS CONFIGURATION $\theta = 30°$

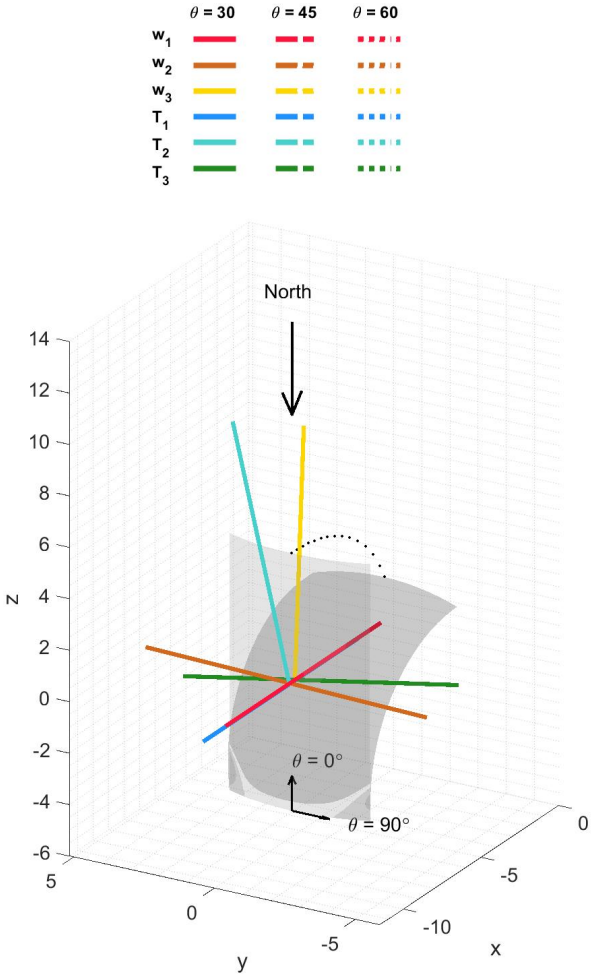

(a)

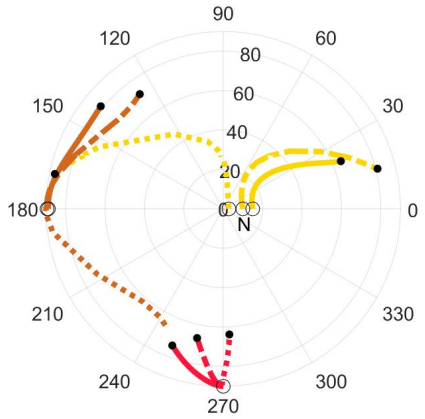

(b)

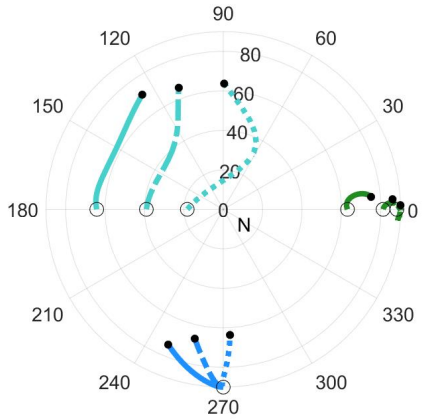

(c)

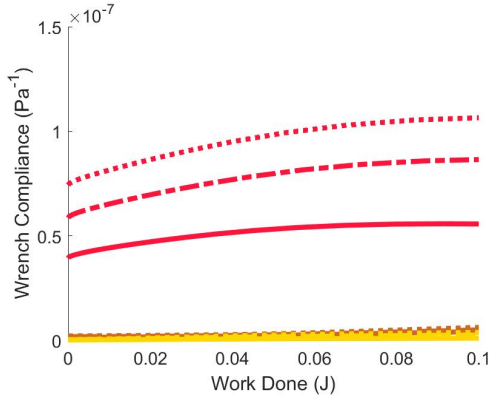

(d)

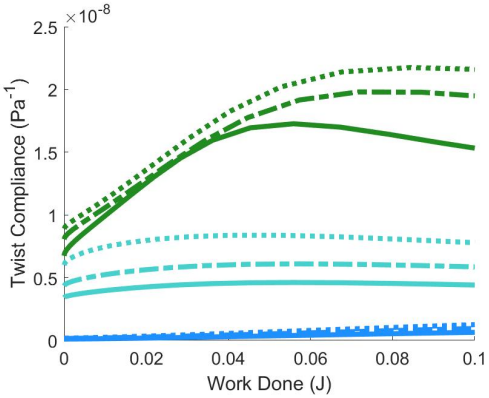

(e)

FIGURE 5: VISUALISATION OF COMPLIANCE BEHAVIOUR FOR SINGLY-CURVED TAPE SPRING ($\beta = 45°$, $a = 2$) SHELL MECHANISMS COMPRISED OF $\theta = 30°$, $\theta = 45°$, OR $\theta = 60°$ LAMINATES. FIGURE (A) SHOWS CONFIGURATION $\theta = 30°$

more drawn out than in Figure 4d, as there is more shell curvature to 'open-out'. This greater 'opening', combined with the favourable twist orientation also increases the peak compliance of T_3. The rotation of w_1 is similar, however, remaining parallel with T_1 (blue), but reflects the reduced overall deformation of the mechanism.

It can be seen that wrenches w_2 (brown) and w_3 (yellow) rotate significantly for this enclosed angle. An interesting phenomena occurs when $\theta = 60°$, as the larger shell curvature causes the axes to rotate in the opposite direction during deformation. As w_2 has very low compliance, this will not affect the shell behaviour greatly, but it is interesting to see how the geometry and stiffness behaviour combine to produce this unexpected effect. Further work is required to identify cases where such effects can occur with more compliant axes.

The magnitudes of twists T_1 and T_2 (teal) remain similar to the $\beta = 15°$ case, although their orientations are subtly different: T_2 rotates, then partially re-aligns throughout deformation, in another case of unusual behaviour resulting from a geometry change. The final orientations of T_2 appear similar, but not identical to, those when $\beta = 15°$. This suggests that the final deformation behaviour is more stiffness-dominated, but that initial deformations are influenced by stiffness and geometry effects: a hybrid response.

With this larger (but not extreme) enclosed angle, more hybrid behaviours occur where initial compliance magnitudes appear to be geometry-dominated, but the axes orientations are noticeably influenced by the fibre angle. The deformation changes from classical tape spring bending, to a non-symmetric bending-torsion which is determined by the stiffness-influenced primary twist orientation. In this hybrid behaviour the primary twist compliance can actually increase as shell curvature 'opens-out'. This effect is prolonged with greater shell curvature, and higher compliance magnitudes can be achieved as rotation around the primary twist axis is more energetically favourable deformation than the classical tape spring bending.

CONCLUSION

A mechanisms characterisation technique by Lipkin and Patterson [1] has for the first time been applied to shell mechanisms with material anisotropy. A visualisation method has been developed to capture the effect of material anisotropy on the magnitude and orientation of the eigen-wrenches and eigen-twists that characterise the mechanical response of a compliant shell mechanism.

Applying this technique to composite tape springs we investigate the interplay between anisotropic alignment and shell geometry. We highlight the visualisation methodology's ability to capture varied response modes and provide physical insight into their mechanical response. We observe how the introduction of anisotropy offers additional modes of mechanism response, expanding the design space, which is of particular value in cases where shell geometry is highly constrained.

Specifically, it highlighted the ability to identify cases where the effects of shell geometry or material anisotropy dominate, as well as when they interact. In addition to this, cases where fibre orientations cause twist and wrench axes to reorient were identified, indicating potential routes for tailoring of shell mechanisms with similar geometry.

Future work will include developing the visualisation method to convey twist and wrench axes locations, which could be of particular relevance for applications such as a scoliosis brace, where the primary twist axis should remain nominally unchanged [9, 10]. In addition, a greater range of shell geometries and degrees of material anisotropy will be investigated (single fibre angle laminates are impractical) to more fully capture the behaviour of shells with different compliances.

ACKNOWLEDGMENT

The work detailed in this paper was funded by the Engineering and Physical Sciences Research Council (EPSRC) as part of the Centre for Doctoral Training in Advanced Composites for Innovation and Science (grant number EP/L016028/1), as well as the National Science Foundation (NSF) (award number 1527133). All data required to reproduce the results shown are provided within this paper.

REFERENCES

[1] Lipkin, H., and Patterson, T., 1992. "Geometrical Properties of Modelled Robot Elasticity: Part I - Decomposition". In Proceedings of the ASME Design Technical Conferences, pp. 179–185.

[2] Howell, L., 2001. *Compliant Mechanisms*. John Wiley & Sons Inc., New York.

[3] Lu, K., and Kota, S., 2003. "Design of Compliant Mechanisms for Morphing Structural Shapes". *Journal of Intelligent Material Systems and Structures,* ***14***(6), pp. 379–391.

[4] Jutte, C., and Kota, S., 2008. "Design of nonlinear springs for prescribed load-displacement functions". *Journal of Mechanical Design,* ***130***(8), p. 081403.

[5] Krishnan, G., Kim, C., and Kota, S., 2013. "A kinetostatic formulation for load-flow visualization in compliant mechanisms". *Journal of Mechanisms and Robotics,* ***5***(2), p. 021007.

[6] Sigmund, O., 1997. "On the design of compliant mechanisms using topology optimization". *Mechanics of Structures and Machines,* ***25***(4), pp. 493–524.

[7] Radaelli, G., and Herder, J., 2014. "Isogeometric Shape Optimization for Compliant Mechanisms With Prescribed Load Paths". In Proceedings of the ASME 2014 Interna-

tional Design Engineering Technical Conferences & Computers and Information in Engineering Conference.

[8] Kooistra, H., Kim, C., van de Sande, W., and Herder, J., 2019. "Shape optimization framework for the path of the primary compliance vector in compliant mechanisms". In Proceedings of the ASME 2019 International Design Engineering Technical Conferences and Computers and Information in Engineering Conference, Vol. V05AT07A00, ASME.

[9] Kooistra, H., 2016. "Scoliosis Brace Design: Utilizing Compliant Shell Mechanisms and Primary Compliance Vector Path Optimization". Master thesis, TU Delft.

[10] Nijssen, J., Radaelli, G., Herder, J., Kim, C., and Ring, J., 2017. "Design and analysis of a shell mechanism based two-fold force controlled scoliosis brace". In Proceedings of the ASME 2017 International Design Engineering Technical Conferences and Computers and Information in Engineering Conference.

[11] Stacey, J., O'Donnell, M., and Schenk, M., 2019. "Thermal Prestress in Composite Compliant Shell Mechanisms". *Journal of Mechanisms and Robotics,* ***11***(2), p. 020908.

[12] Lachenal, X., Daynes, S., and Weaver, P., 2013. "Review of morphing concepts and materials for wind turbine blade applications". *Wind Energy,* ***16***(2), mar, pp. 283–307.

[13] Lamacchia, E., Pirrera, A., Chenchiah, I., and Weaver, P., 2015. "Morphing shell structures: A generalised modelling approach". *Composite Structures,* ***131***, pp. 1017–1027.

[14] Groh, R., and Pirrera, A., 2018. "Extreme mechanics in laminated shells: New insights". *Extreme Mechanics Letters,* ***23***, pp. 17–23.

[15] Dixon, M., O'Donnell, M., Pirrera, A., and Chenchiah, I., 2019. "Bespoke extensional elasticity through helical lattice systems". *Proceedings of the Royal Society A: Mathematical, Physical and Engineering Sciences,* ***475***, p. 20190547.

[16] Li, D., Zhang, X., Guan, Y., and Zhang, H., 2010. "Topology optimization of compliant mechanisms with anisotropic composite materials". In 2010 IEEE International Conference on Mechatronics and Automation, ICMA 2010, IEEE, pp. 416–421.

[17] Tong, X., Ge, W., and Zhang, Y., 2016. "Topology optimization of compliant mechanisms with curvilinear fiber path laminated composites". *Proceedings of the Institution of Mechanical Engineers, Part C: Journal of Mechanical Engineering Science,* ***230***(17), pp. 3101–3110.

[18] Kim, C., 2008. "Functional characterization of compliant building blocks utilizing eigentwists and eigenwrenches". In Proceedings of the ASME 2008 International Design Engineering Technical Conferences & Computers and Information in Engineering Conference.

[19] Krishnan, G., Kim, C., and Kota, S., 2010. "An Intrinsic Geometric Framework for the Building Block Synthesis of Single Point Compliant Mechanisms". *Journal of Mechanisms and Robotics,* ***3***(1), p. 011001.

[20] Nijssen, J., Radaelli, G., Herder, J., Ring, J., and Kim, C., 2018. "Spatial Concept Synthesis of Compliant Mechanisms Utilizing Non-Linear Eigentwist Characterization". In Proceedings of the ASME 2018 International Design Engineering Technical Conferences and Computers and Information in Engineering Conference.

[21] Leemans, J., Kim, C., van de Sande, W., and Herder, J., 2018. "Unified Stiffness Characterization of Nonlinear Compliant Shell Mechanisms". *Journal of Mechanisms and Robotics,* ***11***(1), p. 011011.

[22] Chasles, M., 1831. "Note Sur Les Propriétés Générales du Système de Deux Corps Semblables Entr'eux et Placés D'un Manière Quelconque Dans L'espace; et Sur le Déplacement Fini, ou Infiniment Petit, D'un Corps Solide Libre". *Bulletin Des Sciences Mathématiques, Astronomiques, Physiques et Chimiques,* ***14***, pp. 321–326.

[23] Nettles, A., 1994. Basic mechanics of laminated composite plates. Tech. Rep. October 1994, NASA Marshall Spaceflight Centre.

[24] Daniel, I., and Ishai, O., 2006. *Engineering Mechanics of Composite Materials*, second ed. Oxford University Press, Oxford.

[25] Vannucci, P., and Verchery, G., 2002. "A new method for generating fully isotropic laminates". *Composite Structures,* ***58***(1), pp. 75–82.